Near-infrared reflecting inorganic pigments based on Fe^{3+}-doped TiO_2 prepared via the sol-gel method: characterization and chromatic properties

Zhansong Zhang[1], Haijun Xu[2], Zhiguo Zhou[3], Hesong Hu[4], Tengfei Zhang[5], Zhijie Zhang[6], Mingfeng Zhong[7]
[1, 2, 3]Yuanchuang New Materials and Technology Co., Ltd., Guangzhou, 510440, China
[4]Guangzhou Construction Co., Ltd., Guangzhou, 510030, China
[5, 6, 7]School of Materials Science and Engineering, South China University of Technology, Guangzhou, 510230, China
[2]Corresponding author
E-mail: [1]*402155233@qq.com*, [2]*649727362@qq.com*, [3]*csu_zzhg@163.com*, [4]*39870229@qq.com*, [5]*710748274@qq.com*, [6]*imzhang@scut.edu.cn*, [7]*mfzhong@scut.edu.cn*

Received 25 February 2026; accepted 24 May 2026; published online 16 July 2026
DOI https://doi.org/10.21595/vp.2026.26180

Check for updates

77th International Conference on Vibroengineering in Almaty, Kazakhstan, June 11-12, 2026

Abstract. Novel $Ti_{1-x}Fe_xO_2$ pigments (x = 0-0.2) were successfully synthesized via the sol-gel method. Fe^{3+} doping preserved the rutile phase structure of TiO_2 while suppressing crystal growth; as the Fe content increased, the color of the pigments gradually transitioned from light red to deep red and further to reddish-brown. Among them, $Ti_{0.9}Fe_{0.1}O_2$ calcined at 700 ℃ exhibited the optimal red hue ($a^* = 25.7$), while $Ti_{0.95}Fe_{0.05}O_2$ treated at 800 ℃ demonstrated the best near-infrared reflectance performance (73.62 %). All samples showed notably higher reflectance in the NIR range compared to a commercial iron-oxide pigment of similar color (44.25 %). Furthermore, chromatic property tests after acid/alkali corrosion, together with thermogravimetric-differential scanning calorimetry analysis, confirmed the good chemical and thermal stability of this series of pigments. These energy-saving pigments show promising potential for application in high-efficiency energy-efficient building materials such as solar heat-reflective functional artificial stones.

Keywords: red pigment, TiO_2, Fe^{3+} doping, near-infrared (NIR) reflectance, sol-gel method.

1. Introduction

Energy shortage is a global challenge. Buildings account for roughly 40 % of total energy consumption, with summer cooling making up over one-third of building energy use [1]. To reduce energy consumption and emissions, promoting energy-efficient building materials is essential [2]. Thermal-reflective materials can effectively lower building surface temperatures by reflecting solar radiation [3]. However, most existing options are limited to white or light colors, which show poor stain resistance and fail to meet aesthetic demands for color variety.

Solar radiation consists of 43 % visible light (0.4-0.7 μm), 52 % near-infrared (NIR, 0.7-2.5 μm), and 5 % ultraviolet (0.3-0.4 μm) wavelengths [4]. Crucially, NIR radiation does not affect color perception, and its absorption only causes surface heating. Therefore, by reflecting NIR radiation while preserving the desired visible color, significant heat accumulation can be reduced without compromising aesthetics [5]. Coatings generally contain film-forming agents, additives, and pigments, with pigments playing the most important role in determining the overall solar thermal reflectance. Thus, improving the solar reflectance of pigments is key. Colorful thermal-reflective coatings that incorporate infrared-reflective pigments can retain high solar reflectance compared to conventional coatings of the same color [6], meeting both architectural color requirements and energy-saving objectives [7].

According to the Color Pigment Manufacturers Association (CPMA), commercially available

environmentally friendly red pigments include molybdate red, cadmium red, lead antimonate, bismuth vanadate, ferric ferrocyanide, and complex inorganic pigments (mixed metal oxides). However, these pigments generally exhibit poor solar reflectance. Additionally, some pigments such as $PbCrO_4$, $PbMoO_4$, and CdSe are excluded from commercial use by the CPMA due to their toxicity [8]. Therefore, there is an urgent need to develop novel red inorganic pigments that are both near-infrared (NIR) reflective and environmentally friendly [9-10].

TiO_2 is widely utilized as a coating filler owing to its excellent chemical and thermal stability, high whiteness, and good hiding power. Moreover, rutile-phase TiO_2 demonstrates superior NIR reflectance [11]. Doping TiO_2 offers a promising route for developing colorful pigments that retain high NIR reflectivity. The color of TiO_2 can be tuned via elemental doping, which modifies its electronic band structure and enables selective photon absorption. For example, increasing the concentration of Fe^{3+} doping can shift the color of TiO_2 from white to red [12], making it a potential candidate for high-performance, environmentally benign red pigments.

In this study, we report red pigments based on $Ti_{1-x}Fe_xO_2$ ($x = 0$, 0.05, 0.10, 0.15, and 0.20) synthesized via the sol-gel method at calcination temperatures of 600, 700, 800, and 900 °C. We systematically investigated their crystal structure, surface atomic state, chromatic properties, NIR reflectance performance, and chemical and thermal stability. Finally, this work proposes a novel method for evaluating the comprehensive performance of the colorful energy-saving reflective $Ti_{1-x}Fe_xO_2$ pigments via response surface interaction analysis.

2. Materials and methods

2.1. Synthesis of $Ti_{1-x}Fe_xO_2$ pigments

Synthesis of $Ti_{1-x}Fe_xO_2$ pigments ($x = 0$-0.20) by sol-gel method.

Step 1: Prepare two solutions: Solution A: Take 50 mL tetrabutyl orthotitanate (TBOT, analytically pure) as the titanium source and add it to 100 mL anhydrous ethanol. Then, weigh iron nitrate according to the atomic ratio Ti:Fe (0.97:0.03, 0.095:0.05, 0.92:0.08, 0.9:0.1, 0.85:0.15, 0.8:0.20) and add it to the solution, stir vigorously for 30 minutes. Solution B: Weigh 50 mL of distilled water (Double-distilled water) and 20 mL of glacial acetic acid (analytically pure), add them to 50 mL of anhydrous ethanol, and adjust the pH to 1 with a small amount of nitric acid (analytically pure). Then, stir vigorously for 30 minutes using a magnetic stirrer.

Step 2: Slowly add Solution A to Solution B with stirring, then stir 30 min to form Fe-TiO_2 sol via hydrolysis/condensation.

Step 3: Dry gel at 90 ℃ for 24 h, grind, then calcine in air at varied temperatures for 3 h. Sieve to obtain final pigment powders.

Reference: Commercial iron oxide pigments were used for color comparison.

2.2. Characterization methods

Powder XRD (Bruker D8 ADVANCE) was performed using Cu Kα radiation ($\lambda = 0.15418$ nm) at 40 kV/40 mA. Scans covered 10°-70° 2θ with a step size of 0.02° and 0.2 s per step. Surface composition and chemical states were analyzed with a Shimadzu Axis Ultra DLD spectrometer (Al Kα, 1486.6 eV). The C 1s peak (284.6 eV) served as the energy reference. Analysis chamber pressure was kept at 10^{-9} Pa. Diffuse reflectance spectra (200-2200 nm) were recorded on a Lambda-950 spectrophotometer with an integrating sphere, using PTFE as a reference. NIR solar reflectance (R_s, 700-2500 nm) was calculated according to ASTM G173-03, using the Eq. (1):

$$R_S = \frac{\int_{760}^{2500} R(\lambda) E_\lambda d\lambda}{\int_{760}^{2500} E_\lambda \, d\lambda}, \tag{1}$$

where $R(\lambda)$ is the measured reflectance and $E(\lambda)$ is the solar spectral irradiance from ASTM G173-03.

Color coordinates (L, a, b) were obtained with an X-Rite 8200 colorimeter in CIE Labspace. Chroma (C^*) was calculated as $C^* = \sqrt{(a^*)^2 + (b^*)^2}$. Color change (ΔE^*) was calculated as $\Delta E^* = \sqrt{(\Delta L^*)^2 + (\Delta a^*)^2 + (\Delta b^*)^2}$.Alkali/acid immersion: $Ti_{0.95}Fe_{0.05}O_2$ was immersed in 10 % (w/v) NaOH and 10 % (v/v) HCl separately, stirred 30 min, washed, dried, and weighed to determine mass loss. TG-DSC was performed on a NETZSCH STA449C under N_2 from 50 ℃ to 1000 ℃ at 10 ℃/min, using 9.40 mg of sample.

3. Results and analysis

Fig. 1 presents the XRD patterns of $Ti_{0.95}Fe_{0.05}O_2$ samples calcined at different temperatures (500-1000 ℃) for 3 h. As shown in Fig. 1, the sample calcined at 500 ℃ exhibits a pure anatase phase, while the sample calcined at 600 ℃ shows a mixed phase of anatase and rutile. All samples calcined at temperatures above 700 ℃ are identified as a pure rutile phase.

Fig. 2 presents the XRD patterns of $Ti_{1-x}Fe_xO_2$ samples ($x = 0$ to 0.20) calcined at 700 ℃ for 3 h.

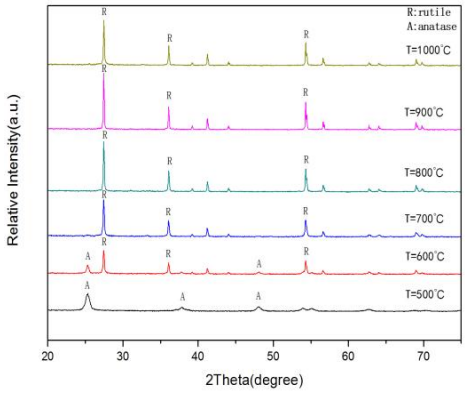

Fig. 1. XRD patterns of $Ti_{0.95}Fe_{0.05}O_2$ samples calcined at different temperatures(left)

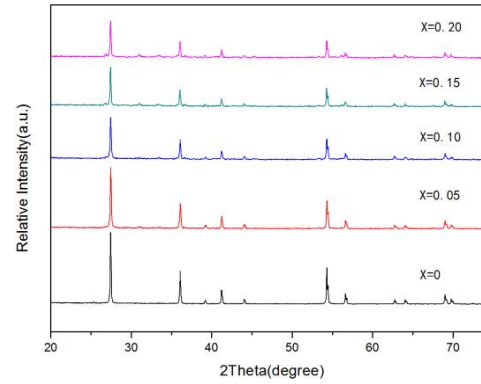

Fig. 2. XRD patterns of $Ti_{1-x}Fe_xO_2$ samples ($x = 0$ to 0.20) calcined at 700 ℃ (right)

Detailed XRD analysis reveals that all diffraction peaks are well-matched with the standard diffraction pattern of rutile-phase TiO_2 (JCPDS card No. 99-0090), and no additional impurity phases are detected. This result indicates that the rutile crystal structure of TiO_2 remains intact with the increase in Fe^{3+} doping content.

The average grain size of $Ti_{0.95}Fe_{0.05}O_2$ samples was calculated from XRD data using the Scherrer equation, and the results are listed in Table 1. It can be seen that the average grain size increases continuously with the elevation of calcination temperature, rising from 11.3 nm at 500 ℃ to 70.4 nm at 1000 ℃.

Table 1. Grain size of $Ti_{0.95}Fe_{0.05}O_2$ powder pigments calcined at different temperatures

T (℃)	500	600	700	800	900	1000
Average grain size (nm)	11.3	41.2	46.6	60.4	66.2	70.4

Table 2 summarizes the average grain size of $Ti_{1-x}Fe_xO_2$ samples ($x = 0$-0.20) calcined at 800 ℃, which shows a gradual decrease with the increase in Fe^{3+} doping content, from 69.4 nm at $x = 0$ to 54.9 nm at $x = 0.20$. This phenomenon suggests that Fe^{3+} doping can effectively inhibit the crystal growth of TiO_2. The underlying reason is that the ionic radius of Fe^{3+} (0.63 Å) is slightly smaller than that of Ti^{4+} (0.68 Å) [11], which disrupts the regular atomic arrangement of the TiO_2

lattice and thus restricts the crystal growth process. Samples sintered at temperatures above 700 ℃ exhibited a pure rutile phase with smaller average particle size compared to those sintered at 800 ℃. Therefore, the sintering temperature for subsequent studies was set at 700 ℃.

Table 2. Grain size of $Ti_{1-x}Fe_xO_2$ (x ranges from 0 to 0.2) powder pigments

X	0	0.05	0.10	0.15	0.20
Average grain size (nm)	69.4	60.4	58.5	55.8	54.9

3.1. XPS analysis

XPS analysis was performed on $Ti_{0.95}Fe_{0.05}O_2$ and undoped TiO_2 samples. The characteristic peaks of the main elements are clearly visible in the wide-scan spectrum (Fig. 3(a)) and the fitted Fe 2p spectrum (Fig. 3(d)), confirming the presence of Fe in the material. The highest peak appears at 532 eV, attributed to the signal of hydroxyl groups in trace organic residues remaining on the sample surface. This peak remains unchanged after doping. Fig. 3(b) compares the high-resolution O 1s spectra of undoped TiO_2 and $Ti_{0.95}Fe_{0.05}O_2$. The stronger peak at 529.5 eV is attributed to metal oxide (O^{2-}) in the TiO_2 lattice. The metal oxide peak of $Ti_{0.95}Fe_{0.05}O_2$ is observed at 530.2eV, which is higher than that of undoped TiO_2 (529.5 eV). This increase in binding energy is attributed to the formation of Fe-O bonds in the lattice [12]. Fig. 3(c) shows the Ti 2p doublet XPS spectra. The Ti $2p_{1/2}$ and Ti $2p_{3/2}$ binding energies of $Ti_{0.95}Fe_{0.05}O_2$ are located at about 465.2 eV and 458.9 eV, respectively, shifting to higher binding energies compared to undoped TiO_2 (464.2 eV and 458.1 eV). The Ti 2p spectra mainly correspond to the Ti^{4+} oxidation state [13]. The observed shifts are attributed to the reduced coordination number of Ti and the shortening of Ti-O bonds, indicating the formation of Fe-O-Ti bonds in the doped sample. In summary, the XPS results confirm the successful incorporation of Fe^{3+} cations into the TiO_2 lattice.

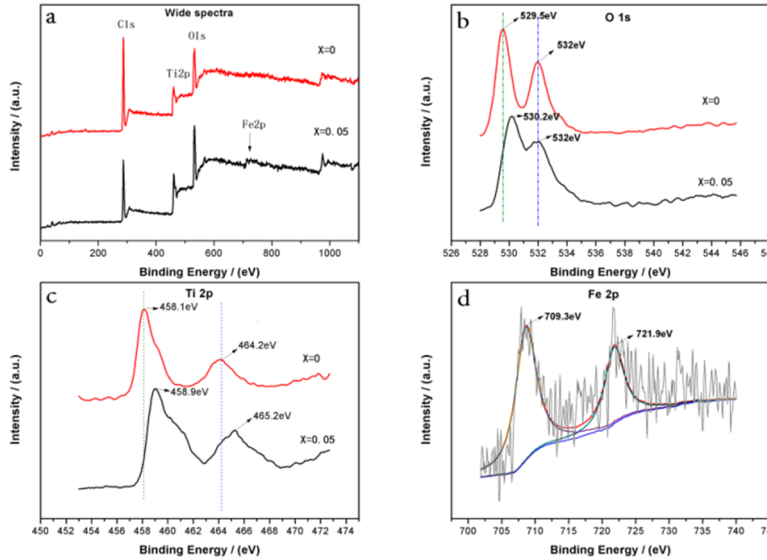

Fig. 3. XPS spectra of the undoped TiO_2 and $Ti_{0.95}Fe_{0.05}O_2$ samples calcined at 800 ℃: a) wide spectra b) O 1s, c) Ti 2p, d) Fe 2p

3.2. Chromatic properties analysis

The CIE 1976 color coordinate values (L^*, a^*, b^*, C^*) of $Ti_{1-x}Fe_xO_2$ samples (x = 0-0.20) calcined at 700 ℃ are presented in Table 3. The chromatic parameters are defined as follows: L^* for lightness, a^* for redness, b^* for yellowness, and C^* for chroma.

It can be clearly seen from Table 3 that with the systematic increase in Fe^{3+} doping content

from $x = 0.05$ to 0.20, the lightness value (L^*) and yellowness value (b^*) of the pigments show a continuous decreasing trend. The redness value (a^*) increases first to the maximum of 25.70 at $x = 0.10$ and then decreases to 20.38 at $x = 0.20$, while the chroma value (C^*) follows the same variation trend as a^*, peaking at 34.89 at $x = 0.10$ and then dropping to 24.77 at $x = 0.20$. As a result, the color tone of the $Ti_{1-x}Fe_xO_2$ pigments changes gradually from light red to deep red and then to brownish red with the increase in Fe^{3+} doping content. The coloring mechanism of the prepared $Ti_{1-x}Fe_xO_2$ pigments is mainly based on the O2p→Ti3d charge transfer transition of the TiO_2 lattice, and this electron transition is further enhanced by the substitution of Ti^{4+} with Fe^{3+} in the TiO_2 crystal structure [14].

Table 3. Color coordinates of $Ti_{1-x}Fe_xO_2$ calcinated at 700 °C and commercial pigment

Iron offered (x)	L^*	a^*	b^*	C^*
0.05	60.00	22.39	25.27	34.14
0.1	50.58	25.70	23.60	34.89
0.15	45.87	21.60	15.86	26.80
0.2	44.38	20.38	14.08	24.77
Commercial pigment	34.57	21.95	11.22	24.65

3.3. NIR reflectance analysis

$Ti_{0.9}Fe_{0.1}O_2$ exhibits the highest color coordinate a^* value. To clarify the correlation between the color and reflectivity of $Ti_{1-x}Fe_xO_2$, further optimization of Fe doping levels was conducted. Table 4 present the color coordinate a^* and NIR solar reflectance values of $Ti_{1-x}Fe_xO_2$ pigments ($x = 0.03$-0.10) calcined at 700 °C, together with the data of the commercial iron oxide pigment for comparison.

Table 4. The detail values of NIR reflectance and color coordinates a^* of $Ti_{1-x}Fe_xO_2$ ($x = 0.03$-0.10)

Pigment composition	$x = 0.03$	$x = 0.05$	$x = 0.08$	$x = 0.10$	Commercial pigment
a^*	15.03	22.39	22.74	25.70	21.95
NIR solar reflectance (%)	74.06	73.62	70.21	62.99	44.25

As shown in Table 4 and Figs.4-5, when the Fe^{3+} doping content increasing from $x = 0.03$ to $x = 0.10$, the NIR solar reflectance of $Ti_{1-x}Fe_xO_2$ pigments shows a continuous decreasing trend from 74.06 % to 62.21 %, and the color coordinate a* value increasing from 15.03 to 25.7. The fundamental reason for this phenomenon is that the valence state of Fe^{3+} is lower than that of Ti^{4+} (the main metal cation in the lattice), and the substitution of Ti^{4+} with Fe^{3+} induces charge imbalance in the TiO_2 lattice, thus promoting the formation of crystallographic point defects (e.g., oxygen vacancies) [15]. With the increase in Fe^{3+} doping content, the number of lattice defects accumulates continuously, which significantly strengthens the absorption of visible light and NIR light and weakens its reflection. Notably, all the prepared $Ti_{1-x}Fe_xO_2$ samples ($x = 0.03$, 0.05, 0.08, 0.10) exhibit a much higher NIR solar reflectance than the commercial iron oxide pigment with similar color (44.25 %).

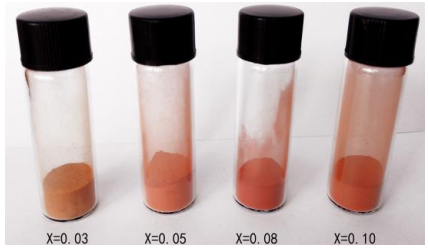

Fig. 4. The pigments photographs of $Ti_{1-x}Fe_xO_2$ ($x = 0.03$-0.10) (left)

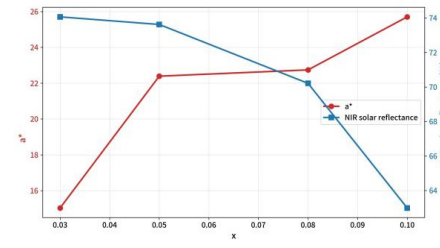

Fig. 5. The relationship between NIR reflectance values and a^* with Fe doping content x (right)

ISSN PRINT 2345-0533, ISSN ONLINE 2538-8479

3.4. Chemical and thermal stability analysis

Table 5 presents the color properties of the pigments after acid/alkali tests, compared with untreated samples, the values of L^*, a^*, and b^* showed minimal differences after washing with 10 % HCl and 10 % NaOH. The total color difference (ΔE^*) was calculated using $\Delta E^* = [(\Delta L^*)^2 + (\Delta a^*)^2 + (\Delta b^*)^2]^{1/2}$. The ΔE^* values was less than 2 % (the qualification requirement ΔE^* for the coating or exterior wall pigment industry is less than 2 %), indicating good chemical stability against the tested acid/alkali. And TG-DSC test results (Fig. 6) showed that the negligible weight change and phase transition indicate that the pigment has good thermal stability.

Table 5. Color coordinates of the $Ti_{0.95}Fe_{0.05}O_2$ after acid/alkali resistance tests

Condition	L^*	a^*	b^*	ΔE^*
Raw	61.55	19.82	25.61	0
10 % HCl	60.41	19.68	25.63	1.14
10 % NaOH	61.43	18.97	24.90	1.11

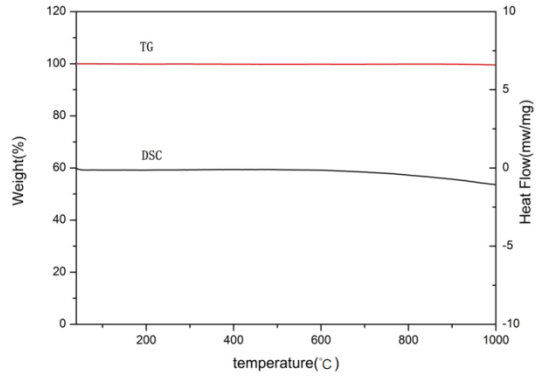

Fig. 6. TG-DSC curves of $Ti_{0.95}Fe_{0.05}O_2$ pigment

4. Conclusions

The $Ti_{1-x}Fe_xO_2$ red pigment series (x = 0-0.20) was successfully synthesized via the sol-gel method. Research shows that the color of the pigments gradually shifts from light red to deep red and eventually to brownish red as the Fe^{3+} doping content increases. Among the samples, $Ti_{0.9}Fe_{0.1}O_2$ calcined at 700 ℃ exhibits the optimal red hue (redness value $a^* = 25.70$), while $Ti_{0.95}Fe_{0.05}O_2$ treated at 700 ℃ demonstrates the best near-infrared reflectance performance (reflectance of 73.62 %). All samples significantly outperform commercially available iron-oxide pigments of similar color (reflectance of 44.25 %). Acid and alkali corrosion resistance tests, along with thermal analysis, further confirm the good chemical and thermal stability of this pigment series. in summary, this energy-saving inorganic pigment, which also possesses solar heat-reflective functionality, shows promising potential for applications in new energy-efficient building materials such as solar heat-reflective artificial stone.

Acknowledgements

The research described in this paper was financially supported by 2022 Science and Technology Innovation Plan Project of Guangdong Provincial Department of Housing and Urban-Rural Development (Grant No 2022-K25-534807), Science and technology planning project of Guangzhou Municipal Construction Group Co., Ltd (Granted No [2022]-KJ009).

Data availability

The datasets generated during and/or analyzed during the current study are available from the corresponding author on reasonable request.

Conflict of interest

The authors declare that they have no conflict of interest.

References

[1] Y. Li, W. Wang, Y. Wang, Y. Xin, T. He, and G. Zhao, "A review of studies involving the effects of climate change on the energy consumption for building heating and cooling," *International Journal of Environmental Research and Public Health*, Vol. 18, No. 1, p. 40, Dec. 2020, https://doi.org/10.3390/ijerph18010040

[2] C. Arumugam and S. Shaik, "Transforming waste disposals into building materials to investigate energy savings and carbon emission mitigation potential," *Environmental Science and Pollution Research*, Vol. 28, No. 12, pp. 15259–15273, Nov. 2020, https://doi.org/10.1007/s11356-020-11693-0

[3] J. Wang, S. Liu, Z. Liu, X. Meng, C. Xu, and W. Gao, "An experimental comparison on regional thermal environment of the high-density enclosed building groups with retro-reflective and high-reflective coatings," *Energy and Buildings*, Vol. 259, p. 111864, Mar. 2022, https://doi.org/10.1016/j.enbuild.2022.111864

[4] T. Kono, Y. Naruse, J. Yamada, and U. M. Rajagopalan, "Exchange of heat radiation between human body and urban environment: characterization in visible, near-infrared, and far-infrared regions," *Applied Sciences*, Vol. 12, No. 20, p. 10412, Oct. 2022, https://doi.org/10.3390/app122010412

[5] A. Lanfranchi, H. Megahd, P. Lova, and D. Comoretto, "Multilayer polymer photonic aegises against near-infrared solar irradiation heating," *ACS Applied Materials and Interfaces*, Vol. 14, No. 12, pp. 14550–14560, 2022, https://doi.org/10.1021/acsami.1c25037

[6] W. Zhang, Y. Zhuang, and Q. Zhang, "Preparation and properties of multi-color coatings with ultra-low near-infrared reflectivity," *Infrared Physics and Technology*, Vol. 136, p. 105122, 2024, https://doi.org/10.1016/j.infrared.2024.105122

[7] K. Lv, X. Liang, L. Zhang, Z. Zhang, and Y. Gao, "A black pigment that shows strong near-infrared reflectivity for solar heat control," *Ceramics International*, Vol. 50, No. 10, pp. 16901–16908, May 2024, https://doi.org/10.1016/j.ceramint.2024.02.164

[8] J. Li, S. Kumari, and M. A. Subramanian, "Solid state inorganic color pigments: ancient to modern," in *Comprehensive Inorganic Chemistry III*, Elsevier, 2023, pp. 560–593, https://doi.org/10.1016/b978-0-12-823144-9.00168-0

[9] V. Elakkiya and S. Sumathi, "Vanadium substituted AlPO4 as environmentally benevolent cool yellow pigment," *Optical Materials*, Vol. 141, p. 113946, 2023, https://doi.org/10.1016/j.optmat.2023.113946

[10] S. Abima and S. Sumathi, "Influence of method of synthesis on the colour and NIR reflective properties of bismuth and vanadium doped cerium phosphate," *Journal of Solid State Chemistry*, Vol. 324, p. 124140, Aug. 2023, https://doi.org/10.1016/j.jssc.2023.124140

[11] A. Mancuso et al., "Photocatalytic degradation of crystal violet dye under visible light by Fe-doped TiO2 prepared by reverse-micelle sol-gel method," *Nanomaterials*, Vol. 13, No. 2, p. 270, 2023, https://doi.org/10.3390/nano13020270

[12] E. H. N. S. Thaines, A. C. Oliveira, L. A. Pocrifka, H. A. Duarte, and R. G. Freitas, "Influence of Fe-doping on the structural and electronic properties of the TiO2 anatase: rutile," the *Journal of Physical Chemistry C*, Vol. 127, No. 46, pp. 22518–22529, 2023, https://doi.org/10.1021/acs.jpcc.3c01780

[13] R. Zhu et al., "Engineering high-efficient phosphorus-doped TiO2 photocatalyst employed for a sophisticated visible-light driven photocatalytic coating," *Progress in Organic Coatings*, Vol. 189, p. 108272, 2024, https://doi.org/10.1016/j.porgcoat.2024.108272

[14] A. Liboon, S. R. Cabo, R. B. Unabia, F. R. G. Bagsican, and R. T. Candidato, "Phase composition, microstructure, and optical characteristics of spin-coated La-TiO2 and Fe-TiO2," *Physica Status Solidi (a)*, Vol. 220, No. 11, p. 2200756, 2023, https://doi.org/10.1002/pssa.202200756

[15] G. Han, J. Y. Kim, K.-J. Kim, H. Lee, and Y.-M. Kim, "Controlling surface oxygen vacancies in Fe-doped TiO2 anatase nanoparticles for superior photocatalytic activities," *Applied Surface Science*, Vol. 507, p. 144916, 2020, https://doi.org/10.1016/j.apsusc.2019.144916